Design of a novel hybrid multimode interferometer operating with both TE and TM polarizations for sensing applications

Yuri H. Isayama[1] · Hugo E. Hernández-Figueroa[2]

Abstract

A novel hybrid multimode interferometer for sensing applications operating with both TE and TM polarizations simultaneously is proposed and numerically demonstrated. The simulations were performed assuming an operating wavelength of 633 nm with the goal of future use as a biosensor, but its applications extend beyond that area and could be adapted for any wavelength or application of interest. By designing the mutimode waveguide core with a low aspect ratio, the confinement characteristics of TE modes and TM modes become very distinct and their interaction with the sample in the sensing area becomes very different as well, resulting in high device sensitivity. In addition, an excitation structure is presented, that allows good control over power distribution between the desired modes while also restricting the power coupled to other undesired modes. This new hybrid TE/TM approach produced a bulk sensitivity per sensor length of 1.798 rad·RIU^{-1} · μm^{-1} and a bulk sensitivity per sensor area of 2.140 rad·RIU^{-1} · μm^{-2}, which represents a much smaller footprint when compared to other MMI sensors, contributing to a higher level of integration, while also opening possibilities for a new range of MMI devices.

Keywords Optical sensors · Optical waveguides · Multimode interferometer · Interferometry

1 Introduction

Throughout the years, medical care has grown in importance in the lives of the population, continuously improving the overall quality of life. One critical challenge is in the field of diagnostic medicine, where there exists the need for reduction of both cost and time required for disease testing in order to achieve early detection of medical conditions (Rezaei et al. 2021). Early detection and diagnosis are very important tools not only in

✉ Yuri H. Isayama
   yurihayama89@gmail.com

1 Center for Semiconductor Components and Nanotechnology, University of Campinas, Campinas, Sao Paulo 13083-870, Brazil

2 School of Electrical and Computer Engineering, Univeristy of Campinas, Campinas, Sao Paulo 13083-852, Brazil

treating symptomatic diseases, but also in a broader sense of health maintenance – a better understanding of disease risk as well as early recognition of deviations from a healthy state allow appropriate interventions (when needed) whatever the disease (Crosby et al. 2020).

Considering the context of the COVID-19 pandemic and the available testing for this disease, diagnostic tests can be divided roughly into two categories: molecular based tests and antigen/antibody tests (Kaur et al. 2021). The first is economically costly and time consuming, due to the need for expensive equipment, well-trained personnel, and well-equipped laboratories (Kaur et al. 2021; Rezaei et al. 2021). The second category has the potential to be simple, rapid, cost-effective, and not require sophisticated facilities, representing a strong candidate for Point-of-Care diagnostics. However, commercially available solutions still suffer from issues like low sensitivity and specificity (Rezaei et al. 2021).

Among the many different types of biosensors, the class of optical ones offers significant advantages in addressing the challenges of Point-of-Care diagnosis. These sensors can be designed to provide characteristics such as rapid (or even real-time) and label-free detection, small footprint and high integration, high sensitivity, and high specificity (Karabchevsky et al. 2020; Kurt et al. 2021; Bekmurzayeva et al. 2021; Arenas et al. 2021). Within this class of optical biosensors, many different technologies and operating mechanisms also exist, each with its strengths and drawbacks, including (but not limited to) Raman Spectroscopy (Zhang et al. 2018), Resonators (Soni et al. 2021), Interferometers (Shamy et al. 2020; Hoppe et al. 2017; Grajales et al. 2019), Leaky Waveguides (Gupta and Goddard 2021), Surface Plasmon Resonance (SPR) (Haider et al. 2021; Ly et al. 2021; Srivastava et al. 2021), and Localized Surface Plasmon Resonance (LSPR) (Chou et al. 2022; Kim et al. 2018). Interferometric biosensors based on Multimode Interferometer (MMI) structures present certain features that attracted interest to this type of device: smaller footprint than other interferometers, integration capabilities allowing multi-analyte sensing, high sensitivity, and label-free detection (Ebihara et al. 2019; Duval et al. 2012; Grajales et al. 2019).

Since its initial conception, in 1999 by Gut et al. (Gut et al. 1999), and the first suggestion of its possible use as a biosensor, by Kribich et al. (Kribich 2005), the planar MMI sensor has undergone several improvements, mostly within biosensing applications: increased sensitivity by use of higher order modes (Ramirez et al. 2015, 2019; Isayama and Hernández-Figueroa 2021), better excitation structures for the propagating modes within the MMI (Liang et al. 2018; Ebihara et al. 2019; Isayama and Hernández-Figueroa 2021), improved light in-coupling in the waveguides (Grajales et al. 2019), incorporation of metal under-cladding in the multimode waveguide structure (Dwivedi and Kumar 2018), and use of slow light enhancing the interaction between light and sample (Torrijos-Morán et al. 2021). In addition, there have been successful demonstrations reported of the use of MMI devices as effective biosensors (Zinoviev et al. 2011; González-Guerrero et al. 2017) and important developments towards Lab-on-Chip capabilities, with the integration of many biosensing structures in the same chip, as seen in Duval et al. (Duval et al. 2012). Even with all these advancements, there is still not only opportunities for improvement, but also demands that emerge from Point-of Care testing requirements.

This paper presents a numerical demonstration of a novel MMI sensor that employs two orthogonal modes, the fundamental Transverse Electric (TE) mode and a high-order Transverse Magnetic mode. This hybrid approach is distinct, to the best of our knowledge, from all MMI biosensors so far reported in the literature. It provides significant increase to device sensitivity, but with a large reduction of footprint, with a bulk sensitivity per sensor length of $1.798 \ \text{rad} \cdot \text{RIU}^{-1} \cdot \mu\text{m}^{-1}$ and a bulk sensitivity per sensor area of $2.140 \ \text{rad} \cdot \text{RIU}^{-1} \cdot \mu\text{m}^{-2}$. Even though other MMI biosensors were able to

produce high sensitivity per sensor length, they were unable to keep a small footprint. In fact, the best MMI biosensor so far in terms of sensitivity per sensor area was the one reported in Ramirez et al. (2015), with 1.131 rad·RIU^{-1} · µm^{-2}. The bulk sensitivity per sensor area obtained in this work represents an improvement of 89% when compared to the best result in the literature to this point.

The paper organization is as follows: initially, the behaviour of the two polarizations, TE/TM, is analyzed and how device performance is affected by combining them within the multimode waveguide; next, the design of an excitation scheme that is able to effectively and efficiently excite the modes in the MMI is demonstrated; considerations on the detection method are made and a performance comparison with other MMI biosensors found in the literature is conducted, considering both sensitivity and footprint; finally, some remarks are made about the fabrication process and experimental measurements, and the conclusions are presented.

2 Multimode interferometer design

Observing the principle of operation of MMI sensors, one may conclude that the device basically compares the propagation of two modes. Each mode present in the MMI have a certain propagation constant (β) and, therefore, is under a different guiding regime. As a consequence, when the sensing area suffers a perturbation due to the presence of the sample (which causes a local variation in the refractive index of the cladding, n_{clad}), each mode's propagation constant changes by a distinct amount and, at the end of the multimode waveguide, each mode will have accumulated a different phase (βL_{MMI}, where L_{MMI} is the length of the MMI). The larger the difference between the propagation constants ($\Delta\beta$) for a given variation of the refractive index of the cladding $\left(\frac{\partial \Delta\beta}{\partial n_{clad}} \right)$ the more sensitive the device. Thus, in order to improve device performance, it is necessary to select a pair of propagating modes that will be affected in the most distinct way when the sensing area is subject to the sample (Isayama and Hernández-Figueroa 2021).

The first and, to the best of our knowledge, only ones to propose a MMI sensor that operated with TE and TM modes were Gut et al., using the fundamental modes TE_{00} and TM_{00} in a planar waveguide, excited by a prism coupler, to monitor the presence of water vapour and ammonia (Gut et al. 1999). With this exception, the rest of developments on MMI biosensors used modes exclusively with either TE polarization or TM polarization. The developments on excitation structures reported in (Isayama and Hernández-Figueroa 2021) allow not only the use of both polarizations within the MMI sensor, but also provide means to effectively and efficiently excite higher order modes as well. Using this excitation scheme, the device of Fig. 1 was devised. There are: two input single-mode waveguides, one with TE and other with TM polarizations; a mode excitation section, where the excitation of the modes of the MMI occur; a sensing region, where the upper cladding is removed so the MMI core may be put into direct contact with the sample; and the output section, where light will exit the device and be interpreted. In the next section, we analyze the properties of TE/TM modes and how they can be combined to create a novel hybrid MMI sensor.
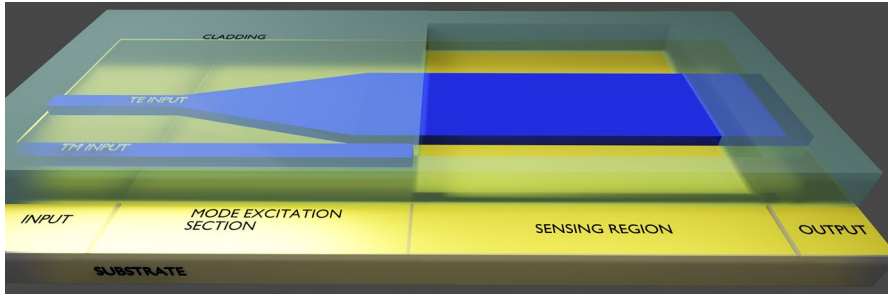
Fig. 1 Schematic of the hybrid MMI sensor

2.1 Combining TE and TM modes

The introduction of the sample in the sensing area produces a local variation of the refractive index of the MMI cladding. This variation changes the propagation constants of the modes within the MMI and the accumulated phase for these modes at the end of the multimode waveguide (output) also changes. If we measure the variation of phase difference at the output, it is possible to infer by how much the refractive index was altered. Bulk sensitivity is a parameter to quantify how sensitive the device is with respect to the changes in the refractive index of the cladding. Defining $\Delta\phi$ as the phase difference between the modes at the output, we know that $\Delta\phi = \frac{2\pi(n_{eff,n}-n_{eff,0})L}{\lambda}$, where $n_{eff,n}$ is the effective index of the nth propagating mode in the MMI, L is the MMI length and λ is the operating wavelength (Ramirez et al. 2015). The bulk sensitivity may, then, be expressed as (Isayama and Hernández-Figueroa 2021)

$$S_{bulk} = \frac{\partial(\Delta\phi)}{\partial n_{clad}} = \frac{2\pi L}{\lambda}\eta_{bulk} \tag{1}$$

$$\eta_{bulk} = \frac{\partial(\Delta n_{eff})}{\partial n_{clad}}, \tag{2}$$

where η_{bulk} is called intrinsic bulk sensitivity.

By analyzing Eq. 1, we conclude that sensitivity is increased when the phase difference highly varies with n_{clad}. This may be achieved if the two propagating modes are affected by the cladding perturbations in very distinct manners. In other words, their guiding regimes must be very different, which leads to them having very different propagation constants. When working with a single polarization (either TE or TM), altering the dimensions of the waveguide core simultaneously changes the propagation characteristics of both propagating modes in the MMI (Ramirez et al. 2015; Isayama and Hernández-Figueroa 2021).

If we introduce two orthogonal modes in the MMI, however, changes in one dimension of the core (width, w, for instance) affect one polarization much more than the other. Figure 2 presents the propagation constants of the fundamental TE mode and several TM modes. The core's height is h = 150 nm while its width is varied from 600 nm to 3200 nm. This waveguide cross-section has a low aspect ratio, which confines better the TE polarization when compared to the TM one. To further comprehend this phenomenon, refer to Fig. 3 that shows the electric field distribution in the cross-section of the MMI for different
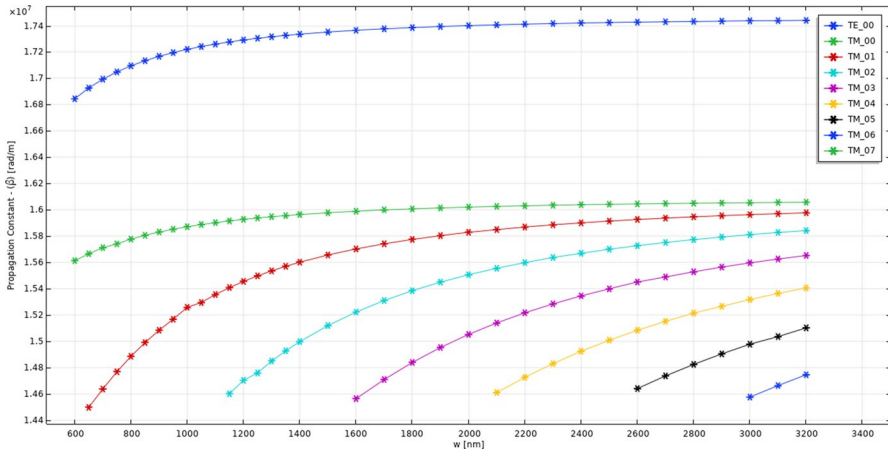
Fig. 2 Propagation constants of TE/TM modes as a function of waveguide core width. Core height is h = 150 nm
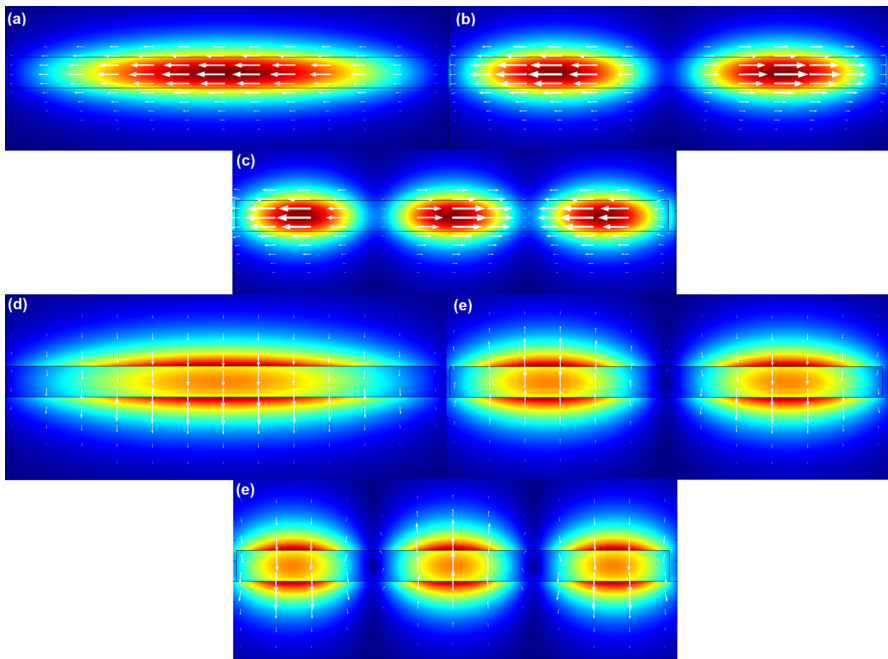

Fig. 3 Electric field distribution (|**E**|) for the modes: **a** TE_{00} **b** TE_{01} **c** TE_{00} **d** TM_{00} **e** TM_{01} **f** TM_{02}. Waveguide core height is h = 150 nm, and width is w = 2.1 μm

propagating modes. For TE modes (Fig. 3a–c, the great majority of their electric field is concentrated within the waveguide core, making these modes present low interaction with the cladding region. As a result, changes in the cladding refractive index will produce very small variations in the propagation constant of TE modes. In contrast, from Fig. 3d–f, one

can see that the TM modes have a very different behaviour: a much smaller portion of the modes' power is confined within the waveguide core, while a great part propagates through the cladding. This characteristic makes the TM modes' interaction with variations in the cladding region much more intense and, as a result, perturbations on the refractive index of the cladding will produce great changes in TM modes' propagation constants. This can also be observed in Fig. 2, where one can compare the propagation constants of the fundamental TE mode with the propagation constants of TM modes. The value of β for the fundamental TE mode is much larger than the values of β for TM modes, meaning that the electromagnetic fields of TM modes are less concentrated in the waveguide core (and more concentrated in the cladding and the substrate) than the TE mode. Therefore, perturbations in the cladding region of the MMI should produce more variations in the propagation constant of TM modes, while not affecting so much the TE polarization. Since the MMI sensor fundamentally compares the propagation of two modes (through the difference in their accumulated phase, $\Delta\beta L$, at the end of the multimode waveguide), by having one mode that has a weak interaction with the sensing area while having another mode with a strong interaction, the value of $\frac{\partial\Delta\phi}{\partial n_{clad}}$ in Eq. 1, and thus the device sensitivity, is expected to be high. In fact, the greater the difference between the two modes' guiding regime, the greater the expected sensitivity.

2.2 Sensitivity calculations

The device design assumed operating wavelength $\lambda = 633$ nm, waveguides composed of Si_3N_4 core (with refractive index $n_{Si_3N_4} = 2.0394$), substrate of SiO_2 ($n_{SiO_2} = 1.4570$), and water cladding ($n_{clad} = 1.3300$). One important remark is that the chosen value for the refractive index of the cladding depends on the application of the designed sensor. In the case of medical applications, such as biosensors for Point-of-Care diagnostics, the samples are mostly aqueous solutions (blood or urine for example) and, therefore, the refractive index of these samples will be close to the one of water. Different applications, such as gas sensing for instance, will require the design to consider a different refractive index for the cladding region.

Calculations of different geometry configurations were performed in the following manner: first, waveguide core parameters were chosen (height, h, and width, w_{MMI}); next, a number of mode analysis with 2D - Finite Element Method (2D-FEM) were conducted to calculate the propagation constants, βs, for TE and TM modes for different values of cladding refractive index (n_{clad} from 1.3200 to 1.4600). The chosen range of values allows the investigation of how the sensor will perform when subject to aqueous based samples, which are of interest in biosensing applications; finally, intrinsic bulk sensitivities were calculated using Eq. 2 for each geometry configuration. The results are shown in Fig. 4. In every device, there are only two propagating modes in the multimode section and the core width, w_{MMI}, was chosen so that the higher order mode is close to cut-off condition, which has been shown to be the best operating condition (Ramirez et al. 2015; Isayama and Hernández-Figueroa 2021). All 2D-FEM simulations were performed with COMSOL Multiphysics. The computational domain simulated was 4 μm in height by 8 μm in width with the waveguide core centered in the domain. Mesh elements were kept to a maximum size of 10.0 nm inside the core and 800 nm outside, but with an element growth rate of 3%, to ensure elements in the vicinity of the core would still be small enough to correctly represent the fields. As the modes of interest are guided modes, the boundary conditions to enclose the computational domain were
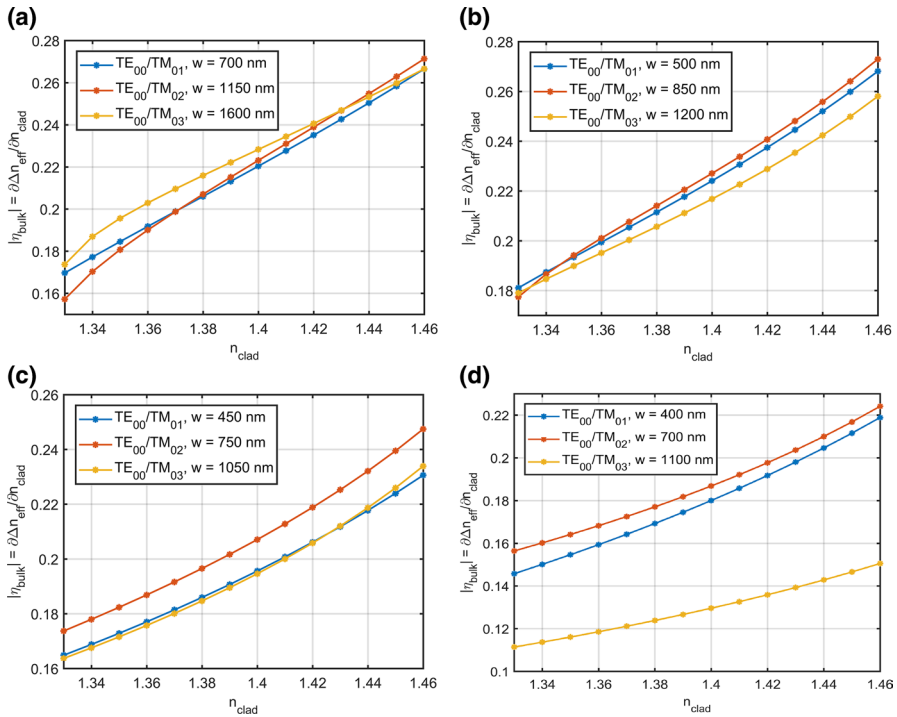
(a)

(b)

(c)

(d)

Fig. 4 Intrinsic bulk sensitivities for different sensor orders and waveguide core height. **a** h = 150 nm. **b** h = 200 nm. **c** h = 250 nm. **d** h = 300 nm

set to be Perfect Electric Conductors (PECs), and the average simulation used meshes with 465,000 elements and the average number of degrees of freedom solved for were 325,000.

Three hybrid MMI sensors are represented in Fig. 4: first order (TE_{00} and TM_{01} modes), second order (TE_{00} and TM_{02} modes) and third order (TE_{00} and TM_{03} modes). From the discussion of Sect. 2.1, the result of reducing the core height is to also reduce the confinement of the propagating modes in the MMI. Because of their symmetry, TM modes are much more affected by changes in the vertical direction of the core than TE modes. Since the MMI sensor essentially compares the accumulated phase of the two propagating modes in the multimode section of the device, the core height reduction will promote a greater difference in the guiding regimes of TE and TM polarizations and by referring to Eqs. 1 and 2, one may see that as the guiding regimes of the two propagating modes in the MMI become more distinct, the bulk sensitivity of the device shall be increased. Reducing the core height also tends to improve device sensitivity because the high order TM mode becomes less confined and is able to interact with the cladding more efficiently, further contributing for the difference in guiding regime when compared to the fundamental TE mode. Nevertheless, there is a limit for this improvement, as the lack of confinement also affects significantly the fundamental TE mode after a certain point. The results presented in Fig. 4 show that when the MMI core height is being reduced from h = 300 nm (Fig. 4d) to 250 nm (Fig. 4c), and then to 200 nm (Fig. 4b), the intrinsic bulk sensitivities kept increasing progressively. However, when

the core height dropped from 200 nm to 150 nm (Fig. 4a), one can observe a decrease in device sensitivity, indicating that the lack of confinement suffered by the fundamental TE mode started to become an important factor.

The best overall performance was presented by the second order hybrid MMI sensor, but specifically for sensing refractive indexes close to 1.33, the first order sensor showed better results (typically, biosensors are required to detect small concentrations of bio-molecules within aqueous solutions and, thus, the expected refractive index for the sample is always very close to water). Furthermore, the detection process and signal interpretation is considerably simpler for the first order sensor, which is essentially the same as the bimodal sensors from the literature (Zinoviev et al. 2011; Grajales et al. 2019). For these reasons, the best design for biosensing applications was elected the first order hybrid MMI sensor with core dimensions of h = 200 nm and w_{MMI} = 500 nm and intrinsic bulk sensitivity of η_{bulk} = 0.1811 RIU^{-1}. The obtained sensitivity will be later compared to the performance of other MMI sensors found in the literature.

3 Excitation structure and detection method

Dimensioning the multimode section of the MMI sensor is one of the steps of the device design. It is also necessary to develop a structure to effectively excite the desired modes within the MMI and understand how to interpret the output signal.

3.1 Excitation of modes in the MMI

There are three important requirements an excitation structure for MMI sensors must fulfil: being able to effectively excite the desired modes (usually a fundamental mode and a higher order one), selectively excite the only two desired modes, and provide good control over the distribution of power between the propagating modes. A strategy similar to (Isayama and Hernández-Figueroa 2021) was employed here, by using a single-mode waveguide and a taper to excite the fundamental TE mode and a second waveguide to excite the first order TM mode through directional coupling.

The first mechanism is straightforward, since size restrictions in optical biosensing are not as demanding as in integrated optics. MMI sensors tend to have several mm in total length, so a few μm long taper is acceptable and, for that reason, a linear taper was adopted. Exciting efficiently the higher mode involves designing the single-mode waveguide so that its propagating mode (the fundamental TM_{00}) has the same β as the TM_{01} of the MMI, making directional coupling possible. Combining these two mechanisms results in the structure depicted in Fig. 5.

For the excitation structure, one must optimize the following parameters: single-mode waveguide width (w_{SMW}), directional coupler length (L_{DC}), directional coupler gap (g_1) and taper length (L_{Taper}). The cladding covering this device section is considered to be SiO_2.

Using 2D-FEM, all parameters were optimized to provide a 50%-50% power distribution between the two propagating modes, TE_{00}/TM_{01}, and to reduce the excitation of other modes to a minimum. The electric field distribution obtained in the simulations is shown in Fig. 6, where it is possible to observe the fundamental TE mode being excited through the taper, Fig. 6b, and the TM_{01} mode being excited through directional coupling, Fig. 6c.

The optimized parameters for the first order hybrid MMI sensor were: w_{MMI} = 500 nm, w_{SMW} = 140 nm, L_{DC} = 5 µm, g_1 = 200 nm and L_{Taper} = 10 μm (linear taper). The power
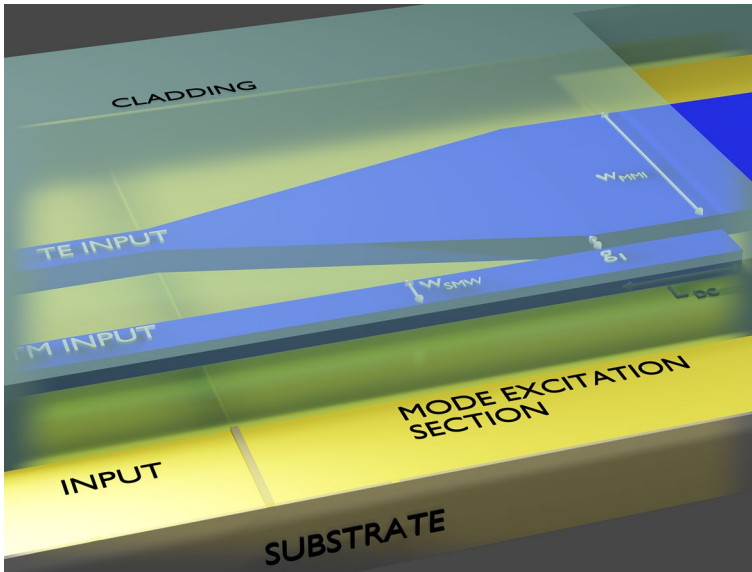
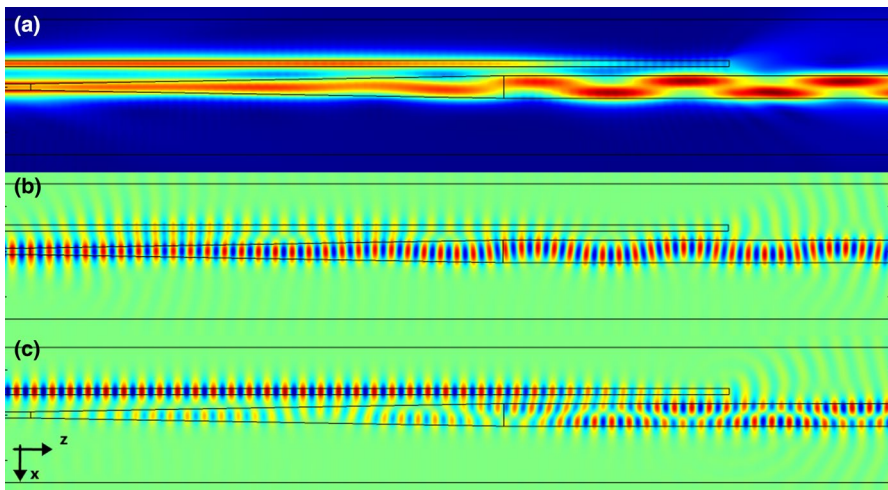**Fig. 5** TE/TM excitation structure

Fig. 6 Electric field distribution within the excitation structure. **a** Total electric field. **b** Parallel component (E_x). **c** Perpendicular component (E_y)

distribution obtained between all possible propagating modes is as follows: 43.32% for the TE_{00} mode; 42.30% for the TM_{01} mode; 4.88% for the TE_{01}mode; and 5.30% for the TM_{00} mode. Some of the input power is coupled to the TE_{01} and the TM_{00} modes, but these powers are one order of magnitude smaller than the two desired modes. In addition, the power distribution between the modes TE_{00} and TM_{01} is roughly 50%-50%, which makes this excitation scheme suitable for the application in question.

3.2 Detection and interpretation of the output signal

The output signal of this sensor will be retrieved from the end of the multimode wave-guide, where we symmetrically position a pair of photodiodes with respect to the center of the waveguide to measure the power coming out of each half of the MMI. Labelling the power measured by each photodiode as $P^{(+)}$ and $P^{(-)}$ we may define the adimensional sensor signal parameter as

$$S(\%) = \frac{P^{(+)} - P^{(-)}}{P^{(+)} + P^{(-)}} \times 100\%. \tag{3}$$

Recalling that $\Delta\phi$ is the phase difference between the two propagating modes, if there is a variation in the refractive index of the cladding within the sensing area of the device, this phase difference will change and the sensor signal will also vary, according to the relation (Duval et al. 2012; Zinoviev et al. 2011)

$$S \propto cos(\Delta\phi) \tag{4}$$

and we may use Eq. 3 to deduce how much was the variation in n_{clad}.

3.3 Comparison with other works in the literature

Referring to Eq. 1, we may see that bulk sensitivity depends on the device length and, the longer the MMI, the higher bulk sensitivity of the sensor. Each work reported in the literature has its particularities and device size (length and width) is one of them. In order to fairly compare the devices in terms of sensitivity it is interesting to consider the bulk sensitivity per sensor length (S_{bulk}/L). Furthermore, if we are interested in integration potential, it is also important to consider the width of the MMI sensor and compare bulk sensitivity per sensor area (S_{bulk}/A), as seen in Table 1.

From Table 1, we note that the hybrid MMI sensor proposed in this work presents the highest bulk sensitivity per sensor length so far obtained by a multimode interference sensor. In terms of sensitivity per sensor length, the hybrid MMI sensor has a slightly better performance than the 4th order MMI sensor reported in (Isayama and Hernández-Figueroa

Table 1 Comparison between MMI sensors in the literature regarding bulk sensitivity per sensor length and area. [1] Isayama and Hernández-Figueroa (2021) [2] Zinoviev et al. (2011) [3] Duval et al. (2012) [4] Ramirez et al. (2015) [5] Liang et al. (2018) [6] Grajales et al. (2019) [7] Ebihara et al. (2019)

Sensor characteristics	S_{bulk}/L $\left[\frac{rad}{RIU\cdot\mu m}\right]$	S_{bulk}/A $\left[\frac{rad}{RIU\cdot\mu m^2}\right]$	References
First order Hybrid Si_3N_4 channel WG	1.798	2.140	This work
4th order Si_3N_4 channel WG	1.787	0.885	[1]
BiMW Si_3N_4 rib WG	0.849	0.283	[2]
BiMW Si_3N_4 rib WG with grating couplers	0.963	0.241	[3]
TriMW Si_3N_4 channel WG	1.131	1.131	[4]
Grating-assisted TriMW ma-P 1205 channel WG	0.859	0.661	[5]
Taper-coupled BiMW Si_3N_4 rib WG	0.901	0.300	[6]
TriMW SU-8 channel WG with DSMW excitation	0.62	0.335	[7]

2021). Until now, the MMI sensor that provided the best compromise between sensitivity and footprint was the TriMW Si_3N_4 channel WG from Ramirez et al. (Ramirez et al. 2015). Even though it did not present the highest sensitivity, it was the device which allowed better efficiency in terms of integration of multiple sensors in a single chip. However, the hybrid MMI sensor proposed in this work provides not only the highest sensitivity in the literature, but also presents the best candidate in terms of integration capacity: its simple and compact excitation structure combined with a narrower multimode section–total device width is 840 nm for the hybrid MMI sensor compared to 1.0 µm for the TriMW Si_3N_4 channel WG of (Ramirez et al. 2015) – results in an enhancement in sensitivity per sensor area of 89.2% compared to the best MMI device reported so far. This allows the possibility for a much greater integration level, which is an important feature for future developments in Lab-on-Chip technologies.

Another relevant sensor characteristic is the Limit-of-Detection (LOD), which can be defined as (Zinoviev et al. 2011)

$$LOD = \frac{3 \cdot N/S}{S_{bulk}},\tag{5}$$

where N/S is the Noise-to-Signal ratio.

Because the experimental setting necessary to the first order hybrid MMI sensor is essentially the same as the one described in (Zinoviev et al. 2011), if we assume the same values of $3 \cdot N/S = 5 \cdot 10^{-4} 2\pi$ and sensor length $L_{MMI} = 1.5$ mm, the estimated LOD for this new sensor is $1.15 \cdot 10^{-7}$ RIU^{-1}. The obtained value is even comparable to other technologies recently reported, such as fiber optics SPR (LOD = $4.3 \cdot 10^{-6}$ RIU^{-1} (Kaur et al. 2021)), photonic crystal sensors (LOD = $1.92 \cdot 10^{-6}$ RIU^{-1} (Gandhi et al. 2021)) and nanoplasmonic sensors (LOD = $3 \cdot 10^{-8}$ RIU^{-1} (Lotfiani et al. 2022)).

3.4 Some brief remarks on fabrication and experimental aspects

From an experimental point of view, the main advantages of this hybrid MMI sensor can be pointed as: silicon nitride is a well-established platform for optical devices, which provides a wide range of strategies for both fabrication and optical characterization of the devices; and both in-chip light coupling and sensor output acquisition and processing that are required have experimental demonstrations in the literature.

In terms of fabrication requirements, the processes needed are basically the same ones explored for planar waveguide fabrication using silicon nitride platforms. One example is the work of Sacher et al. (2019), where they describe a method for fabricating Si_3N_4 waveguides with core heights between 135 nm and 200 nm, and core widths that can be as small as ~200 nm, with operating wavelengths in the visible range of the spectrum. They also managed to obtain low propagation losses for these waveguides, which is an important feature. As the sensitivity of any MMI sensor depends on the length of the multimode waveguide, the longer the device the better (Ebihara et al. 2019). However, as propagation losses become higher, the output sensing signal also becomes weaker, increasing the Noise-to-Signal ratio. But as propagation losses increase exponentially with the device length, while sensitivity only increases linearly, from Eq. 5 it is expected to exist a certain device length that maximizes the LOD.

Regarding the experimental setup needed, firstly there is the in-chip light coupling step. Different approaches can be employed such as vertical tapers (Grajales et al. 2019) or grating couplers (Zhu et al. 2017), for instance. One important design decision,

though, is how to obtain both TE and TM polarizations in the chip, which are needed to excite the modes in the Hybrid MMI sensor. One might choose to utilize two separate structures to couple each mode separately, or a polarization rotator could be implemented within the chip. One example of the latter strategy is the work performed by Gallacher et al. (2022), where they demonstrated a polarization rotator for visible wavelengths in silicon nitride platform with good mode conversion characteristics and relatively short device length ($\sim$1000 μm). Finally, in terms of output signal processing, the experimental setup needed is the same as in Zinoviev et al. (2011), where the output light from the MMI may be captured with a two sectional photodiode and the procedure for phase difference calculation is described in Sect. 3.2.

4 Conclusions

In this paper, we propose a novel hybrid TE/TM MMI sensor, which operates with the fundamental TE mode and the first order TM mode, for sensing applications. This device is based on the fact that TE and TM modes present highly distinct propagation constants when the aspect ratio of the core is very low. As a result, their guiding regime is different and perturbations on the refractive index of the multimode waveguide cladding also affect both modes in a different manner, improving the sensitivity of the MMI device. An excitation scheme is also presented, introducing the possibility of utilizing orthogonal modes while providing good control over the power distribution between the two desired modes and reducing to a minimum the power coupled to undesired modes as well. For bulk refractive indexes close to 1.33, the estimated LOD is $1.15 \cdot 10^{-7}$ RIU^{-1}, which is a better result than the other MMI biosensors in the literature and also comparable to other biosensor technologies. In addition, the compact structure of the hybrid MMI sensor produced an enhancement of 89.2% sensitivity per sensor area when compared to the best MMI sensor in the literature. The employment of orthogonal modes within the biosensor structure also opens possibilities for a new range of optical sensors.

 Data availability The authors confirm that the data supporting the findings of this study are available within the article.

Declarations

Conflict of interest The authors have no relevant financial or non-financial interests to disclose.

Ethical approval Not applicable.

References

Arenas, Ángela Écija., Kirchner, E.-M., Hirsch, T., Fernández-Romero, J.M.: Development of an aptamer-based spr-biosensor for the determination of kanamycin residues in foods. Anal. Chim. Acta. **1169**, 338631 (2021)

Bekmurzayeva, A., Ashikbayeva, Z., Myrkhiyeva, Z., Nugmanova, A., Shaimerdenova, M., Ayupova, T., Tosi, D.: Label-free fiber-optic spherical tip biosensor to enable picomolar-level detection of cd44 protein. Sci. Rep. **11**, 19583 (2021)

Chou, H.-T., Liao, Y.-S., Wu, T.-M., Wang, S.-H., Su, W.-C.: Development of localized surface plasmon resonance-based optical fiber biosensor for immunoassay using gold nanoparticles and graphene oxide nanocomposite film. IEEE Sens. J. **22**(7), 6593–6600 (2022)

Crosby, D., Lyons, N., Greenwood, E., Harrison, S., Moffat, J., et al.: A roadmap for the early detection and diagnosis of cancer. Lancet Oncol. **21**(11), 1397–1399 (2020). https://doi.org/10.1016/S1470-2045(20)30593-3

Duval, D., González-Guerrero, A.B., Dante, S., Osmond, J., Monge, R., Fernández, L.J., Lechuga, L.M.: Nanophotonic lab-on-achip platforms including novel bimodal interferometers, microfluidics and grating couplers. Lab Chip **12**, 1987–1994 (2012). https://doi.org/10.1039/C2LC40054E

Dwivedi, R., Kumar, A.: Refractive index sensing using silicon-oninsulator waveguide based modal interferometer. Optik **156**, 961–967 (2018)

Ebihara, K., Uchiyamada, K., Asakawa, K., Okubo, K., Suzuki, H.: Trimodal polymer waveguide interferometer for chemical sensing. Japanese J. Appl. Phys. **58**(6), 062005 (2019). https://doi.org/10.7567/1347-4065/ab2221

Gallacher, K., Griffin, P.F., Riis, E., Sorel, M., Paul, D.J.: Silicon nitride waveguide polarization rotator and polarization beam splitter for chip-scale atomic systems. APL Photonics **7**, 046101 (2022)

Gandhi, S., Awasthi, S.K., Aly, A.H.: Biophotonic sensor design using a 1d defective annular photonic crystal for the detection of creatinine concentration in blood serum. RSC Adv. **11**, 26655–26665 (2021)

González-Guerrero, A.B., Maldonado, J., Dante, S., Grajales, D., Lechuga, L.L.: Direct and label-free detection of the human growth hormone in urine by an ultrasensitive bimodal waveguide biosensor. J. Biophotonics **1**, 61–67 (2017)

Grajales, D., Gavela, A.F., Domínguez, C., Sendra, J.R., Lechuga, L.M.: Low-cost vertical taper for highly efficient light in-coupling in bimodal nanointerferometric waveguide biosensors. J. Phys. Photonics **1**, 025002 (2019). https://doi.org/10.1088/2515-7647/aafebb

Gupta, R., Goddard, N.J.: A study of diffraction-based chitosan leaky waveguide (LW) biosensors. Analyst **146**, 4964–4971 (2021)

Gut, K., Karasiński, P., Wójcik, W., Rogoziński, R., Opilski, Z., Opilski, A.: Applicability of interference te0-tm0 modes and te0-te1 modes to the construction of waveguide sensors. Optica Applicata **29**, 101–110 (1999)

Haider, F., Ahmmed Aoni, R., Ahmed, R., Jen Chew, W., Amouzad Mahdiraji, G.: Plasmonic micro-channel based highly sensitive biosensor in visible to mid-ir. Opt. Laser Technol. **140**, 107020 (2021)

Hoppe, N., Föhn, T., Diersing, P., Scheck, P., Vogel, W., Rosa, M.F., Berroth, M.: Design of an integrated dual-mode interferometer on 250 nm silicon-on-insulator. IEEE J. Select. Top. Quantum Electron. **23**(2), 444–451 (2017). https://doi.org/10.1109/JSTQE.2016.2618602

Isayama, Y.H., Hernández-Figueroa, H.E.: High-order multimode waveguide interferometer for optical biosensing applications. Sensors (2021). https://doi.org/10.3390/s21093254

Karabchevsky, A., Katiyi, A., Ang, A.S., Hazan, A.: On-chip nanophotonics and future challenges. Nanophotonics (2020). https://doi.org/10.1515/nanoph-2020-0204

Kaur, G., Gupta, M., Aggarwal, A., Sagar, V.: Diagnosis of covid-19 An evolution from hospital based to point of care testing. J. Commun. Med. Public Health (2021). https://doi.org/10.29011/2577-2228.100212

Kaur, B., Kumar, S., Kaushik, B.K.: 2d materials-based fiber optic spr biosensor for cancer detection at 1550 nm. IEEE Sens. J. **21**(21), 23957–23964 (2021)

Kim, H.-M., Park, J.-H., Jeong, D.H., Lee, H.-Y., Lee, S.-K.: Real-time detection of prostate-specific antigens using a highly reliable fiber-optic localized surface plasmon resonance sensor combined with micro fluidic channel. Sens. Actuators B: Chem. **273**, 891–898 (2018). https://doi.org/10.1016/j.snb.2018.07.007

Kribich, K.R., et al.: Novel chemical sensor/biosensor platform based on optical multimode interference (mmi) couplers. Sens. Actuators B: Chem. **107**, 188–192 (2005)

Kurt, H., Pishva, P., Pehlivan, Z.S., Arsoy, E.G., Saleem, Q., Bayazıt, M.K., Yüce, M.: Nanoplasmonic biosensors: theory, structure, design, and review of recent applications. Analytica Chimica Acta **1185**, 338842 (2021)

Liang, Y., Zhao, M., Wu, Z., Morthier, G.: Investigation of grating-assisted trimodal interferometer biosensors based on a polymer platform. Sensors **18**(5), 1502 (2018). https://doi.org/10.3390/s18051502

Lotfiani, A., Dehdashti Jahromi, H., Hamedi, S.: Monolithic silicon-based photovoltaic-nanoplasmonic biosensor with enhanced limit of detection and minimum detectable power. J. Lightw. Technol. **40**(4), 1231–1237 (2022)

Ly, T.T., Ruan, Y., Du, B., Jia, P., Zhang, H.: Fibre-optic surface plasmon resonance biosensor for monoclonal antibody titer quantification. Biosensors **11**(10), 383 (2021)

Ramirez, J.C., Gabrielli, L.H., Lechuga, L.M., Hernández-Figueroa, H.E.: Trimodal waveguide demonstration and its implementation as a high order mode interferometer for sensing application. Sens. (Basel) **19**(12), 2821 (2019)https://doi.org/10.3390/s19122821

Ramirez, J.C., Lechuga, L.M., Gabrielli, L.H., Hernandez-Figueroa, H.E.: Study of a low-cost trimodal polymer waveguide for interferometric optical biosensors. Opt. Express **23**(9), 11985–11994 (2015)

Rezaei, M., Razavi Bazaz, S., Zhand, S., Sayyadi, N., Jin, D., Stewart, M.P., Ebrahimi Warkiani, M.: Point of care diagnostics in the age of covid-19. Diagnostics **11**(1), 9 (2021)

Sacher, W.D., Luo, X., Yang, Y., Chen, F.-D., Lordello, T., Mak, J.C.C., Poon, J.K.S.: Visible-light silicon nitride waveguide devices and implantable neurophotonic probes on thinned 200 mm silicon wafers. Opt. Express **27**, 37400–37418 (2019)

Shamy, R.S.E., Khalil, D., Swillam, M.A.: Mid infrared optical gas sensor using plasmonic mach-zehnder interferometer. Sci. Rep. **10**, 1293 (2020). https://doi.org/10.1038/s41598-020-57538-1

Soni, V., Chang, C.-W., Xu, X., Wang, C., Yan, H., D'Agati, M., Chen, R.T.: Portable automatic microring resonator system using a subwavelength grating metamaterial waveguide for high-sensitivity realtime optical-biosensing applications. IEEE Trans. Biomed. Eng. **68**(6), 1894–1902 (2021). https://doi.org/10.1109/TBME.2020.3029148

Srivastava, A., Sharma, A.K., Kumar Prajapati, Y.: On the sensitivityenhancement in plasmonic biosensor with photonic spin hall effect at visible wavelength. Chem. Phys. Lett. **774**, 138613 (2021)

Torrijos-Morán, L., Griol, A., García-Rupérez, J.: Slow light bimodal interferometry in one-dimensional photonic crystal waveguides. Sci. Appl. Light **10**, 16 (2021)

Zhang, L., Li, X., Wang, Y., Sun, K., Chen, X., Chen, H., Zhou, J.: Reproducible plasmonic nanopyramid array of various metals for highly sensitive refractometric and surface-enhanced raman biosensing. ACS Omega **3**(10), 14181–14187 (2018). https://doi.org/10.1021/acsomega.7b02016

Zhu, Y., Wang, J., Xie, W., Tian, B., Li, Y., Brainis, E., Thourhout, D.V.: Ultra-compact silicon nitride grating coupler for microscopy systems. Opt. Express **25**, 33297–33304 (2017)

Zinoviev, K.E., González-Guerrero, A.B., Domínguez, C., Lechuga, L.M.: Integrated bimodal waveguide interferometric biosensor for label-free analysis. J. Lightw. Technol. **29**(13), 1926–1930 (2011)